Research Article | Vol. 11, No. 10 / 1 October 2020 / Biomedical Optics Express 5982
Biomedical Optics EXPRESS

Depth-resolved Mueller matrix polarimetry microscopy of the rat cornea

V. N. Du Le,[1,3] Ilyas Saytashev,[2] Sudipta Saha,[1] Pedro F. Lopez,[2] Megan Laughrey,[2] and Jessica C. Ramella-Roman[1,2,4]

[1]Department of Biomedical Engineering, College of Engineering and Computing, Florida International University, 10555 West Flagler Street, Miami, FL 33174, USA
[2]Department of Ophthalmology, Herbert Wertheim College of Medicine, Florida International University, 11200 SW 8th Street, Miami, FL 33199, USA
[3]vidule@fiu.edu
[4]jramella@fiu.edu

Abstract: Mueller matrix polarimetry (MMP) is a promising linear imaging modality that can enable visualization and measurement of the polarization properties of the cornea. Although the distribution of corneal birefringence has been reported, depth resolved MMP imaging of the cornea has not been archived and remains challenging. In this work, we perform depth-resolved imaging of the cornea using an improved system that combines Mueller matrix reflectance and transmission microscopy together with nonlinear microscopy utilizing second harmonic generation (SHG) and two photon excitation fluorescence (TPEF). We show that TPEF can reveal corneal epithelial cellular network while SHG can highlight the presence of corneal stromal lamellae. We then demonstrate that, in confocal reflectance measurement, as depth increases from 0 to 80 μm both corneal depolarization and retardation increase. Furthermore, it is shown that the spatial distribution of corneal depolarization and retardation displays similar complexity in both reflectance (confocal and non-confocal) and transmission measurement, likely due to the strong degree of heterogeneity in the stromal lamellae.

1. Introduction

Mueller matrix polarimetry (MMP) has been implemented to characterize the polarization properties of biological tissues such as the human eye [1–3], the cervix [4,5], and cardiac tissues [6,7]. Polarization properties such as depolarization and retardation may carry morphological, structural, and compositional information of the tissues [2,8]. MMP has been used extensively in the determination of orientation and retardation of fibrous tissues due to its sensitivity to anisotropic structures as found in the cornea [3,9–12]. The polarization properties of the cornea arise from the structural organization of its constituents such as fibrils and lamellae [13–21].

Although reflectance imaging of the cornea is crucial in the diagnosis of eye diseases, it is particularly challenging due to its relatively high transparency in the visible and near-infrared spectral regions [22]. Corneal birefringence also remains a critical parameter for any polarimetric approach to quantify biological changes (such as glucose level) [1] or physical changes (due to ocular surgery) in the eye [19]. The corneal structure is depth dependent, consisting of: the superficial epithelium, the basal epithelium, the Bowman layer, the anterior and posterior stroma, and the endothelium [17,23]. While rat corneal thickness can range between 120 μm and 150 μm [24,25], the stroma contributing 90% of the corneal thickness is composed of hundreds of lamellae and is responsible for most of the eye birefringence [16,26]. Yet there is very little understanding of the polarization properties differences between corneal epithelium and stroma besides what was provided by polarization-sensitive optical coherence tomography (PS-OCT) [27].

#402201 https://doi.org/10.1364/BOE.402201
Journal © 2020 Received 7 Jul 2020; revised 15 Sep 2020; accepted 21 Sep 2020; published 30 Sep 2020

Biomedical Optics EXPRESS

In context of quantifying the corneal birefringence parameters, MMP may have advantages over other polarimetric imaging methods such as polarized microscopy, PS-OCT and scanning laser polarimetry (SLP). Specifically, polarized microscope has limited depth-resolved access to provide the orientations of collagen fibers in the plane of the sample and it only works well for systems where retardance is the only significant polarimetric effect [26] whereas SLP may give inaccurate result of retardance in systems with high depolarization and diattenuation effects [28,29], and PS-OCT utilizing the Jones formalism provides limited information about the degree of depolarization of partially polarized light [30,31].

The adaptation of Mueller matrix ellipsometry for direct measurement of retinal polarization properties was first reported by van Blokland using a photo multiplier tube detector [32]. Motivated by van Blokland's studies, several groups have incorporated Mueller matrix imaging for studying the polarization properties of the eye. Bueno *et al.* have developed a camera-based Mueller matrix imaging polarimetry to study *in vitro* cornea and *in vivo* eye [33]. Mueller matrix imaging polarimetry has also been incorporated to SLP for contrast enhancement in retinal imaging [34,35] and high quality retinal imaging [36]. Lara and Dainty have designed an axially-resolved Mueller matrix confocal microscopy using multiple channel photodetector scheme [37,38] . They used a double-pass eigen-value calibration method [39], and to show the feasibility of constructing Mueller matrices at different depths of a sample. Although previous MMP studies have reported that there is an increase of corneal retardation when distance from the corneal apex increases in all radial directions [16,26], to our knowledge there are no investigations on depth-resolved corneal birefringence measurements using MMP except our group previous limited assessment [40].

This paper aims to quantitatively investigate the depth-resolved changes of rat corneal birefringence using an improved Mueller matrix polarimetric microscopy system [40] that enables both transmission and reflectance measurement. Nonlinear signals including second harmonic generation (SHG) and two photon excitation fluorescence (TPEF) were also measured. SHG can highlight the presence of collagen fibers which dominate the measurements of retardation and depolarization [41] whereas TPEF defines intracellular space by NAD(P)H fluorescence, and TPEF with DAPI-staining can highlight cellular nuclei. The rationale of our method is to utilize SHG and TPEF non-linear optical signals to validate the information obtained from the back-reflectance confocal and transmission measurement through the Mueller matrix derived depolarization and retardance parameters. We then demonstrate that corneal layered-specific changes in the order of micrometer can strongly affect its polarization properties.

2. Material and methods

The imaging system used in this study is an improvement of what proposed in [40] and it is shown in Fig. 1. The SHG (with 400 ± 30 nm bandpass filter) and TPEF (with 500 ± 20 nm bandpass filter) images are constructed by averaging 100 images for each of the channels, leading to better signal to noise ratio. The new system has the three additional channels/photomultiplier tubes (PMT3, PMT4, and PMT5) enabling the measurement of transmission, confocal and non-confocal (total) reflectance signals. Note that the camera in previous set-up was replaced with the confocal channel with a physical pinhole of diameter 25 μm. MMP imaging is enabled by using a polarization state generator (PSG) at the microscope input, a polarization state analyzer (PSA) before PMT3&4 and another PSA before PMT5. Both PSA and PSG consist of a pair of liquid crystal variable retarders (LCVRs, Meadowlark Optics, Frederick, CO) and a linear polarizer (LPNIR100, Thorlabs Inc., Newton, NJ) oriented parallel to the reference plane (optical bench). All six LCVRs are operated by two D3040 USB controllers (Meadowlark Optics, Frederick, CO). A Mueller matrix is constructed from four different polarization state analyzer (PSA) states for each of the six-polarization state generator (PSG) states, resulting in a set of 24

Biomedical Optics EXPRESS

images in each of the three channels. Depth precision is archived with a stepper motor translation stage (MCM 3000, Thorlabs Inc., Newton, NJ).

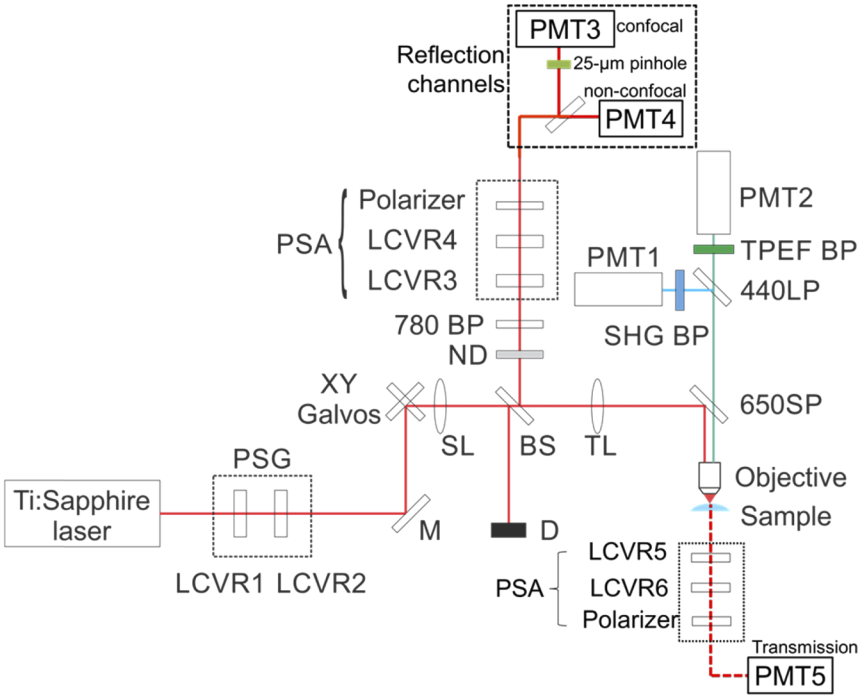

Fig. 1. Schematic diagram of the improved nonlinear and MMP laser scanning microscope. SHG and TPEF was collected with PMT1 and PMT2. A pair of liquid crystal variable retarders (LCVR1 and LCVR2) deliver six polarization states calibrated at the focal point of the 20X objective (Nikon Plan Apo 20X/0.75 DIC M/N2). In reflectance measurement, a fraction of a reflected signal from a sample is attenuated (ND), filtered (BP filter), further analyzed by another pair of liquid crystal variable retarders (LCVR3 and LCVR4) with a polarizer, and then acquired by the confocal and non-confocal reflectance PMTs (PMT3&4). In transmission measurement, another pair of LCVR5 and LCVR6 with a polarizer is used to analyze the transmitted signal which then collected by PMT5. D: beam dumps, BS: beam splitter, ND: neutral density filter, BP: bandpass filter, SL: scan lens, TL: tube lens, SP: short-pass filter

The detailed description of the system and the methods of Mueller matrices calculation and decomposition can be found elsewhere [40,42].

In this work, rat corneas were removed from fresh rat eyes, and imaging was performed at central cornea within one day at room temperature (21°C). The rat eyes were obtained from fresh rat carcasses donated from other the Institutional Animal Care and Use Committee (IACUC) approved protocols at Florida International University. The cornea can be either unstained or DAPI-stained. The unstained corneas were mounted on a glass slide using the optimal cutting temperature (OCT) embedding medium (Fisher Scientific, Pittsburgh, PA) whereas the stained corneas were mounted on a glass slide using DAPI (ThermoFisher Scientific, Grand Island, NY). TPEF, SHG, depolarization (Δ), total retardation (total R), total intensity (M_{11}) of each sample are reported. In this paper, we show some example images and analysis of rat corneas, including one DAPI stained sample.

Biomedical Optics EXPRESS

3. Results

3.1. DAPI-stained cornea

In order to confirm the presence of epithelial cells, imaging of DAPI-stained rat corneal sample was performed first. Figure 2 shows 2-D images of the stained cornea as depth increases from 0 to 50 μm. In rat cornea, cells are densely packed in the superficial and basal epithelium whereas collagen fibrils are found in the stromal lamellae [17]. As expected, TPEF channel shows tightly packed cellular nuclei in the corneal epithelium at depth of 0 and 10 μm. They appear brightly due to the strong two-photon excitation fluorescence of DAPI around 500 nm [43,44]. The stained nuclei have diameter between 5 and 6.5 μm, resembling cellular nuclei in corneal basal epithelium [23]. Meanwhile, SHG signal marks the presence of collagen in the stromal lamellae [44,45] and this signal is increasing with depth, particularly beyond 10 μm (Fig. 2). Using SHG

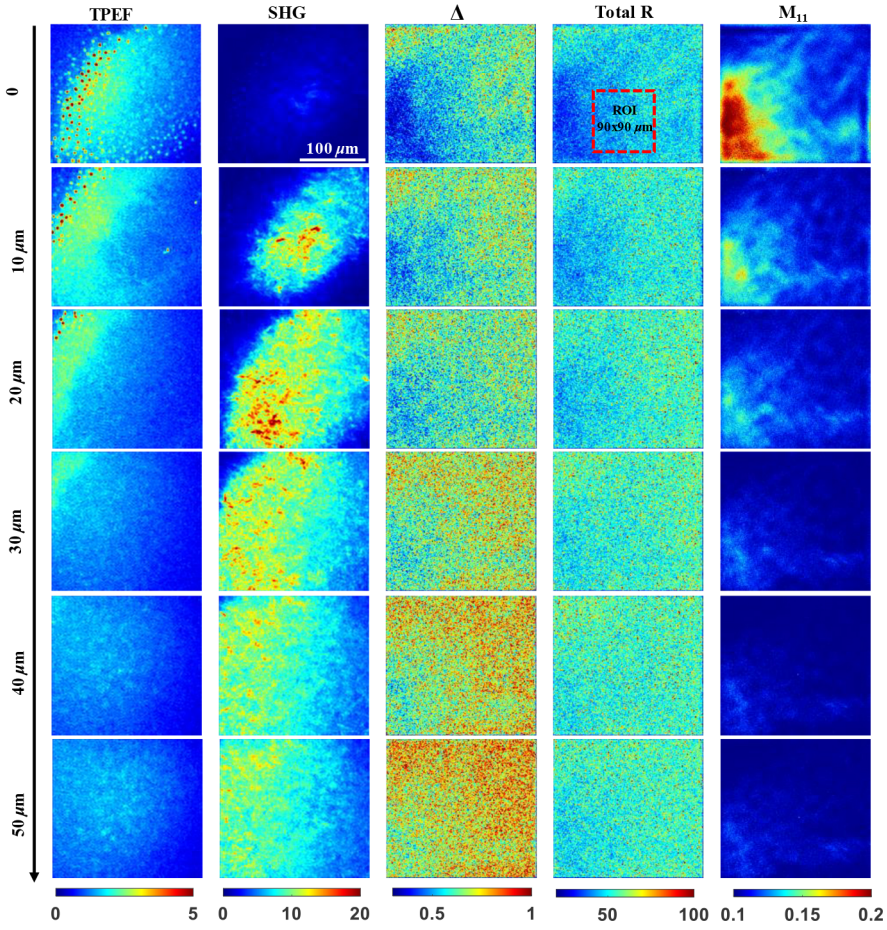

Fig. 2. Depth-resolved images of a DAPI-stained rat cornea sample from confocal reflectance channel reveal cellular structure at top layers (up to 10 μm depth), and an increase of collagen (increase in SHG) as depth increases. The diameter of stained nuclei observed in TPEF channel at 0 μm depth is between 5 and 6.5 μm, resembling cellular nuclei in corneal basal epithelium [23]. The stromal collagen is visualized at beyond 10 μm depth.

Biomedical Optics EXPRESS

as ground truth for polarimetry images, it is also observed that both depolarization (Δ) and total confocal retardation (total R) are increasing with depth.

Quantitative analysis of the DAPI-stained sample is shown in Fig. 3. The percentage change represents the relative change in signal to the first imaging plane at depth 0 μm. A negative change indicates a decrease in intensity. As depth (d) increases from 0 to 20 μm, SHG increases approximately 80% while Δ and total R only increases about 5% and 7%, respectively, and TPEF decreases approximately 10% (Fig. 3). Notably, SHG remains constant between depth of 20 and 50 μm. Comparing between depth of 0 and of 60 μm, SHG increases approximately 65% whereas TPEF decreases approximately 12%.

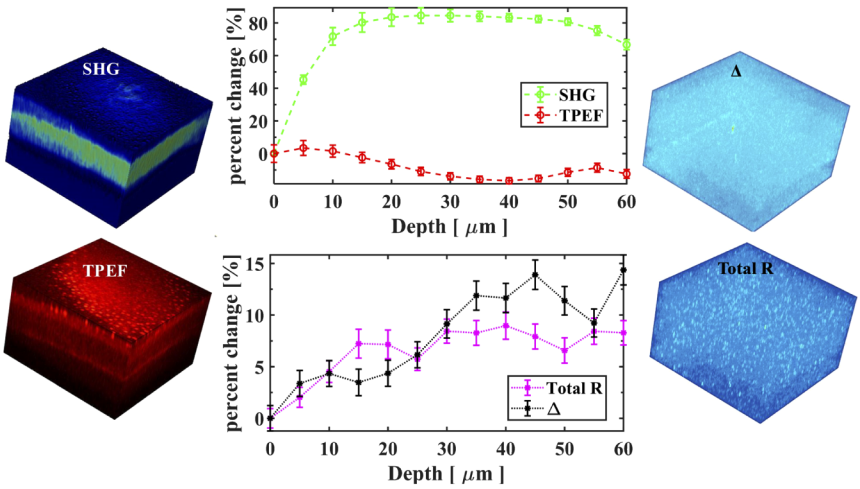

Fig. 3. Quantitative analysis of nonlinear and MMP signal of DAPI-stained rat cornea in Fig. 2: 3-D cube represents volume of data and graph represents percentage change in signal for the selected ROI in Fig. 2. SHG confirms collagen in basal epithelium and stroma whereas TPEF confirms cellular structure in corneal epithelium Changes in SHG also confirms the changes in polarization properties with an increase in both Δ and total R. Error bar represents standard error.

In Fig. 3, volume rendering method was used to generate the 3-D volumes for SHG and TPEF whereas maximum intensity projection (MIP) was used to generate the 3-D volumes for Δ and total R. Specifically, volume rendering utilizes intensity map to adjust image opacity of SHG and TPEF data while MIP reveals the highest intensity value for each imaging planes of Δ and total R data.

3.2. Unstained cornea

Imaging and quantitative analysis of two unstained corneal samples are shown next (Figs. 4–7) to demonstrate the label-free utility of the technique. In the first unstained cornea sample (Figs. 4 and 5), TPEF imaging at the top layer shows structures resembling the basal epithelium whereas both TPEF and SHG images of the bottom layers (beyond 40 μm depth) indicate the anterior and posterior stromal lamellae [17,23]. At shallow depth, SHG, Δ and total R are increasing. Interestingly, at depth greater than 30 μm, both SHG and Δ remain constant while total R is increasing (Fig. 4). A region of interest (ROI) was selected for quantitative analysis. From depth of 0 to 90 μm, the analysis of ROI shows that TPEF decreases approximately 30%, while SHG, Δ, total R increases approximately 25%, 15%, and 45%, respectively (Fig. 5).

Images of the second rat cornea are shown in Figs. 6&7. Figure 6 shows the 2-D images of the in confocal reflectance channel and Fig. 7 shows analysis for the ROI in Fig. 6. Like Fig. 2, Fig. 6

Biomedical Optics EXPRESS

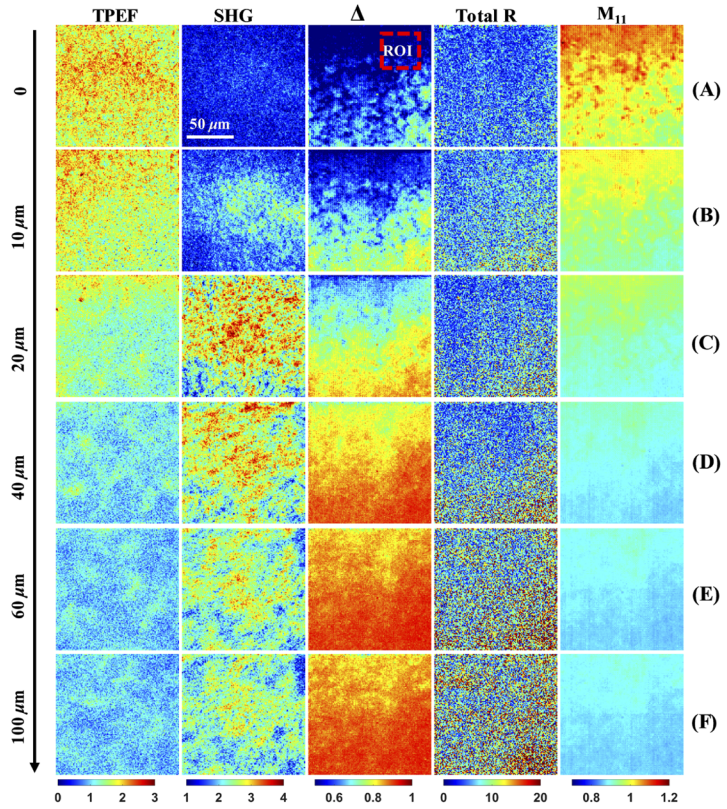

Fig. 4. Depth-resolved images of unstained rat cornea from confocal reflectance channel: TPEF at top layers (A&B) reveals cellular network that resembles basal epithelium whereas SHG at bottom layers (D-F) represents the anterior and posterior stromal lamellae. Changes in SHG also confirms the changes in polarimetry images with an increase in both Δ and total R.

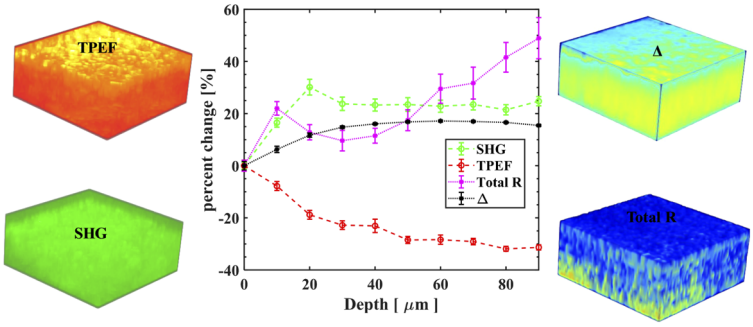

Fig. 5. Quantitative analysis of nonlinear and MMP images in Fig. 4: 3-D cube represents volume of data whereas plot shows analysis of only ROI in Fig. 4. SHG remains high depth above 40 μm, confirming presence of collagen into deep stroma [17]. TPEF decreases with depth, consistent with the observed trend in DAPI-stained sample.

Biomedical Optics EXPRESS

shows that TPEF is strong at top layer and decreases with depth, and that SHG is strong beyond depth of 10 μm, likely due to the presence of collagen in the stromal lamellae.

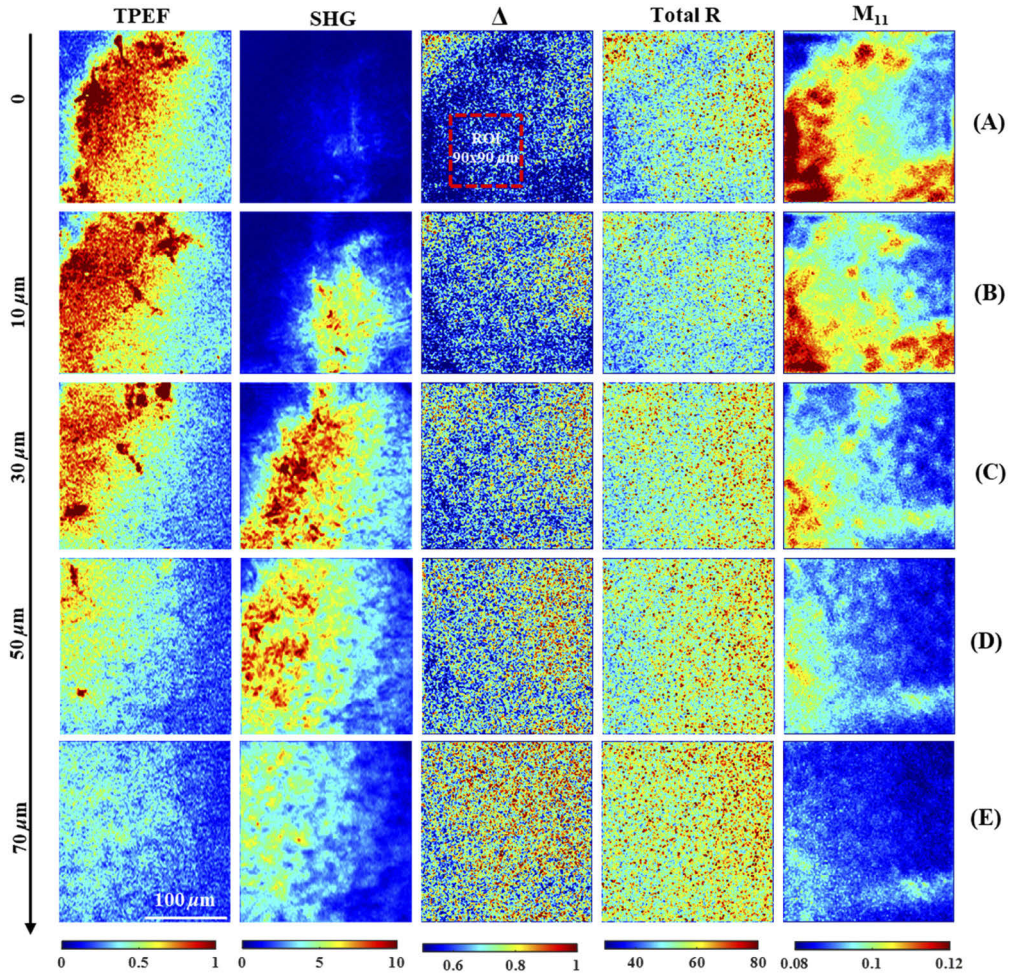

Fig. 6. Another rat cornea sample measured with confocal reflectance channel: TPEF and SHG reveals the Bowman layer with subepithelial nerve plexus at 0-5 μm depth (C-D), and the epithelium-stroma interface at 15 μm. Selected region of interest (ROI, 90×90 μm^2) is used for quantitative analysis in Fig. 7.

The selected ROIs at depth of 10 and 70 μm are shown in Fig. 7 to give a better visualization. ROIs of both TPEF and SHG show a strong degree of heterogeneity at shallow depth and at deeper region of rat cornea. The relative complexity was also observed in the maps of depolarization and retardation (Fig. 7). From depth of 0 to 80 μm, SHG increases by 43% while Δ and total R only increases approximately 10%and 5%, respectively, and TPEF decreases approximately 40% (Fig. 7).

Images at depth of 10 μm and 70 μm from transmission measurement of the same rat cornea was showed in Fig. 8. M_{11} confirms the presence of corneal epithelial cellular network while map of Δ and total R demonstrates the strong degree of heterogeneity as seen in confocal reflectance measurement.

Images at depth of 10 μm and 70 μm from non-confocal (total) reflectance measurement of the same cornea (Figs. 5–7) are shown in Fig. 9. Maps of Δ and total R in non-confocal reflectance

Biomedical Optics EXPRESS

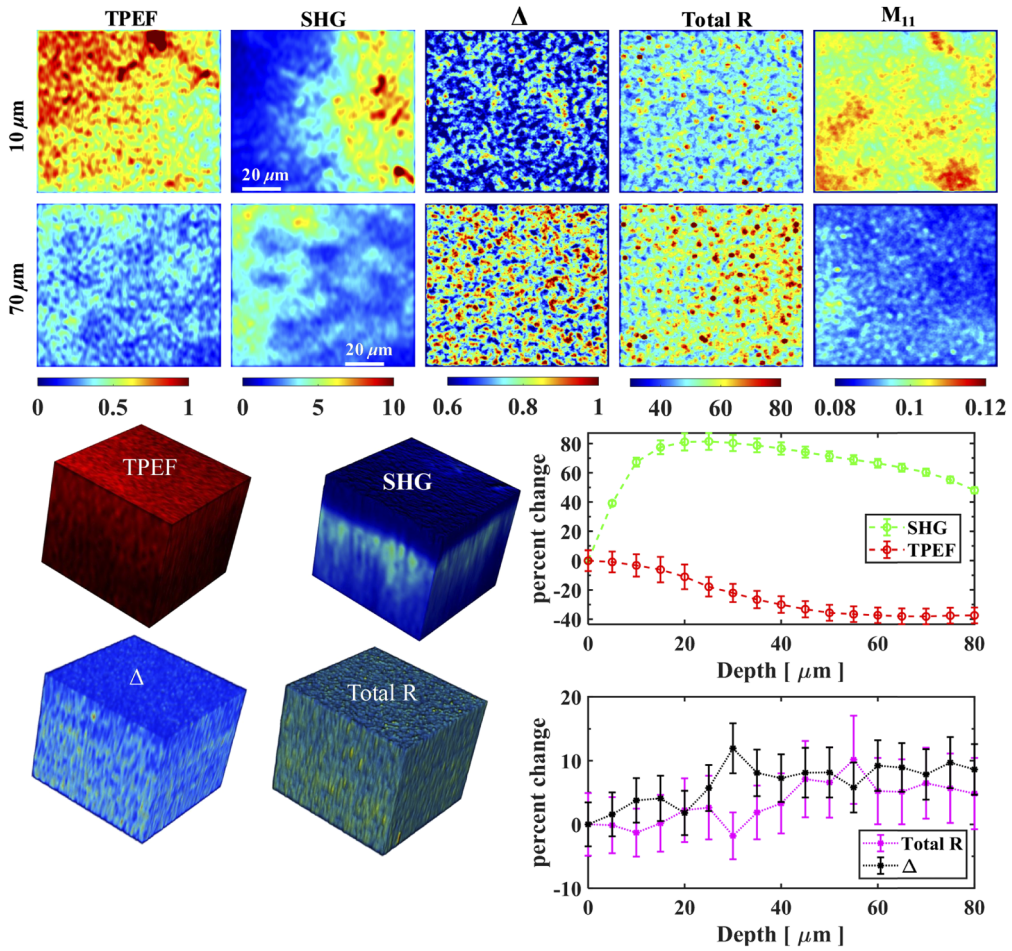

Fig. 7. Quantitative analysis for ROI in Fig. 6: Top two rows show images at 10 and 70 μm depth whereas bottom row shows 3-D volume of SHG and TPEF, and percent change. Overall, retardation and depolarization do not change significantly with depth. Imaging maps however clearly show stronger degree of spatial retardation and depolarization 70 μm depth.

Biomedical Optics EXPRESS

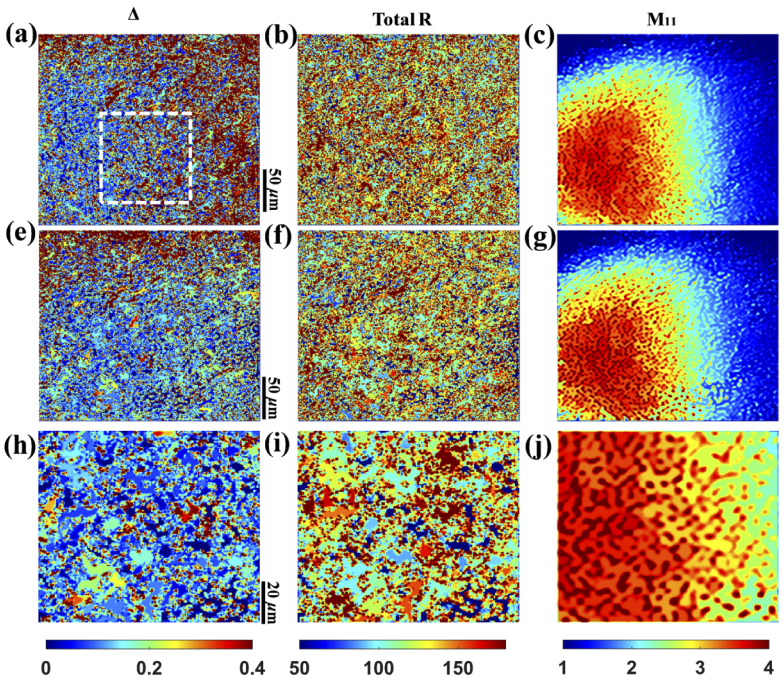

Fig. 8. Images from transmission channel for the same cornea sample as in Fig. 6 at depth of 10 μm (a-c) and 70 μm (e-g). The bottom images (h-j) are zoomed in ROI (90×90 μm^2) in (a-c). No significance changes in Δ and total R as depth increases. M_{11} shows similar cellular network to that of epithelium.

measurement describe a similar degree of heterogeneity seen in confocal reflectance measurement. Quantitative analysis for both transmission and non-confocal reflectance measurement was shown in Fig. 10. In contrast to confocal measurements (Figs. 3&5&7), no significance change (less than 6% and well within errors) in Δ and total R was observed when the sample was moved from confocal imagery in both transmission and non-confocal reflectance measurements.

Biomedical Optics EXPRESS

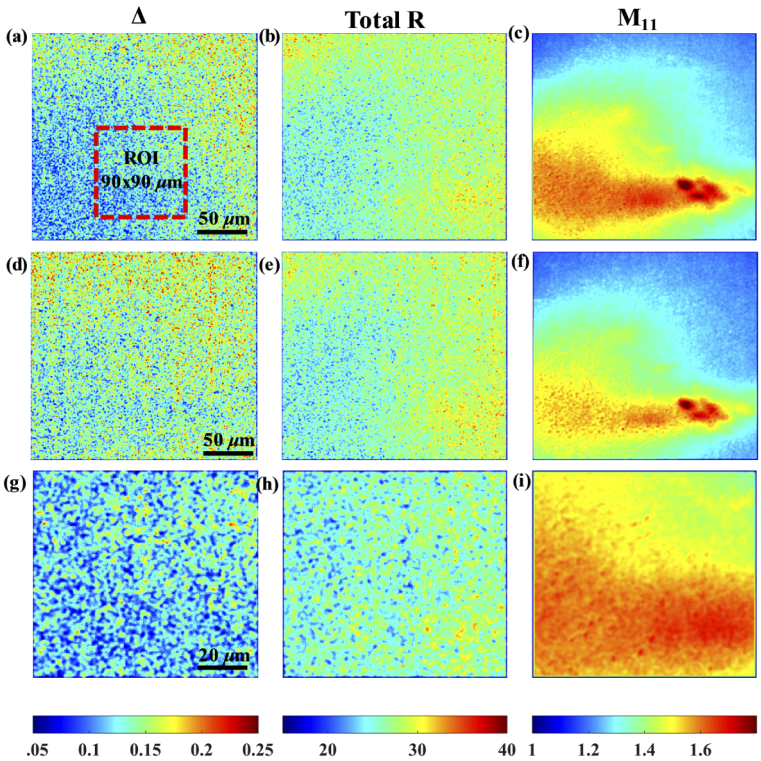

Fig. 9. Images from non-confocal reflectance channel for the same cornea sample as in Fig. 5 at depth of 10 μm (a-c) and 70 μm (e-g). The bottom images (h-j) are zoomed in ROI (90×90 μm^2) in (a-c). No significance changes in Δ, total R and M_{11} as depth increases. Zoomed in images (g-i) display similar complexity in Δ and total R as shown in Fig. 7.

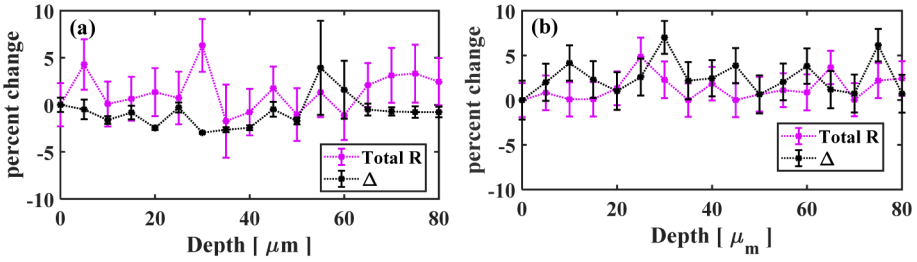

Fig. 10. Quantitative analysis for ROIs in Figs. 8&9 from 0 to 80 μm depth: (a) transmission and (b) non-confocal reflectance measurement. In compared to the trends shown in Fig. 3&5&7 for confocal reflectance measurement, no significant changes in Δ and total R were observed as depth increases.

4. Discussion and conclusion

We have measured the effect of cellular and collagen distribution on the polarization properties of the rat cornea through depth-resolved confocal MMP. TPEF images of DAPI-stained cornea reveals densely packed cellular nuclei with diameter between 5 and 6.5 μm, resembling cellular nuclei in corneal basal epithelium [23] while SHG images show strong collagen features, marking the corneal epithelium-stroma interface and the presence of the stromal lamellae. We showed that as depth increases SHG signal can increase up to 80% whereas TPEF can decrease 40%. Also,

Biomedical Optics EXPRESS

both depolarization and retardation increase with depth in confocal reflectance measurement. In the samples shown in this paper, the percentage change in depolarization was approximately10% from 0 to 80 μm depth (Figs. 3&7). This number was 40% for total retardation (Fig. 5).

Whereas these are average values, the polarization heterogeneity can be noted in the images and volume rendering both in xy and z direction. Although this spatial heterogeneity has been noted by others across the cornea, it has not been directly correlated with local biological components such as cellular nuclei and collagen. Such correlation is particularly relevant when the local properties influence the overall measured metric, such as assessing glucose level in the aqueous humor. Optical rotation by glucose has been measured as few as millidegrees which makes its decoupling from the overall signal extremely challenging. Westphal *et al.* [1] used transmission elastography at different wavelengths and reported the Mueller Matrix values across several regions of the cornea. They showed that birefringence is dependent on angle of incidence and the sampled region. They noted that even small movement in the patient eye would cause the changes in the light-cornea interaction zone. In this paper, we showed visually how the spatial changes are connected to different biological structures within the cornea, and our findings are consistent with what was reported previously. PS-OCT studies showed depolarization properties is lower in the corneal epithelium, and higher in corneal stroma [27]. Dias and Ziebarth have also shown that bulk collagen lamellae structure in the corneal stroma strongly affect the reflection of polarized light, resulting in spatial variation in corneal birefringence [45]. Finally, we also report the spatial distribution of polarization properties is similar in complexity in total transmission and reflectance measurement.

In this work, we have demonstrated that heterogeneity of the stromal lamellae is responsible for complicated spatial variation of corneal polarization properties. One critical note is that we were able to show the distribution of both depolarization and retardation in the cornea in 3-D with a direct link to local biological structures.

Funding

National Science Foundation (DMR 1548924); Herbert and Nicole Wertheim Professorship Endowment (all authors).

Acknowledgments

We are grateful to Jeff Gomes for preparing the rat tissues. We are thankful for the supports from Herbert Wertheim College of Medicine, Florida International University.

Disclosures

The authors declare no conflicts of interest.

References

1. P. Westphal, J. M. Kaltenbach, and K. Wicker, "Corneal birefringence measured by spectrally resolved Mueller matrix ellipsometry and implications for non-invasive glucose monitoring," Biomed. Opt. Express **7**(4), 1160–1174 (2016).
2. V. V. Tuchin, "Polarized light interaction with tissues," J. Biomed. Opt. **21**(7), 071114 (2016).
3. N. Ghosh and I. A. Vitkin, "Tissue polarimetry: concepts, challenges, applications, and outlook," J. Biomed. Opt. **16**(11), 110801 (2011).
4. J. Vizet, J. Rehbinder, S. Deby, S. Roussel, A. Nazac, R. Soufan, C. Genestie, C. Haie-Meder, H. Fernandez, F. Moreau, and A. Pierangelo, "In vivo imaging of uterine cervix with a Mueller polarimetric colposcope," Sci. Rep. **7**(1), 2471 (2017).
5. A. Pierangelo, A. Nazac, A. Benali, P. Validire, H. Cohen, T. Novikova, B. H. Ibrahim, S. Manhas, C. Fallet, M.-R. Antonelli, and A.-D. Martino, "Polarimetric imaging of uterine cervix: a case study," Opt. Express **21**(12), 14120–14130 (2013).
6. S. D. Giattina, B. K. Courtney, P. R. Herz, M. Harman, S. Shortkroff, D. L. Stamper, B. Liu, J. G. Fujimoto, and M. E. Brezinski, "Assessment of coronary plaque collagen with polarization sensitive optical coherence tomography (PS-OCT)," Int. J. Cardiol. **107**(3), 400–409 (2006).

Biomedical Optics EXPRESS

7. M. A. Wallenburg, M. Pop, M. F. G. Wood, N. Ghosh, G. A. Wright, and I. A. Vitkin, "Comparison of Optical Polarimetry and Diffusion Tensor Mr Imaging for Assessing Myocardial Anisotropy," J. Innovative Opt. Health Sci. **03**(02), 109–121 (2010).
8. V. Backman, R. Gurjar, K. Badizadegan, I. Itzkan, R. Dasari, L. T. Perelman, and M. S. Feld, "Polarized light scattering spectroscopy for quantitative measurement of epithelial cellular structures in situ," IEEE J. Sel. Top. Quantum Electron. **5**(4), 1019–1026 (1999).
9. N. Ghosh, M. Wood, and I. A. Vitkin, "Polarized Light Assessment of Complex Turbid Media Such as Biological Tissues Using Mueller Matrix Decomposition," Ser. Med. Phys. Biomed. **20102371**, 253–282 (2010).
10. V. V. Tuchin, "Handbook of Optical Sensing of Glucose in Biological Fluids and Tissues," Handbook of Optical Sensing of Glucose in Biological Fluids and Tissues, Xvii-Xxvi (2009).
11. M. F. G. Wood, N. Ghosh, M. A. Wallenburg, S. H. Li, R. D. Weisel, B. C. Wilson, R. K. Li, and I. A. Vitkin, "Polarization birefringence measurements for characterizing the myocardium, including healthy, infarcted, and stem-cell-regenerated tissues," J. Biomed. Opt. **15**(4), 047009 (2010).
12. V. F. Izotova, I. L. Maksimova, I. S. Nefedov, and S. V. Romanov, "Investigation of Mueller matrices of anisotropic nonhomogeneous layers in application to an optical model of the cornea," Appl. Opt. **36**(1), 164–169 (1997).
13. R. W. Knighton, X.-R. Huang, and L. A. Cavuoto, "Corneal birefringence mapped by scanning laser polarimetry," Opt. Express **16**(18), 13738–13751 (2008).
14. R. A. Bone and G. Draper, "Optical anisotropy of the human cornea determined with a polarizing microscope," Appl. Opt. **46**(34), 8351–8357 (2007).
15. J. M. Bueno and J. Jaronski, "Spatially resolved polarization properties for in vitro corneas," Oph. Phys. Optics. **21**(5), 384–392 (2001).
16. J. M. Bueno and F. Vargas-Martin, "Measurements of the corneal birefringence with a liquid-crystal imaging polariscope," Appl. Opt. **41**(1), 116–124 (2002).
17. J. T. Henriksson, A. M. McDermott, and J. P. Bergmanson, "Dimensions and morphology of the cornea in three strains of mice. Investigative ophthalmology & visual science," Invest. Ophthalmol Vis. Sci. **50**(8), 3648–3654 (2009).
18. R. W. Knighton, "Spectral dependence of corneal birefringence at visible wavelengths," Invest. Ophthalmol. Visual Sci. **43**, U26 (2002).
19. J. M. Bueno, "The influence of depolarization and corneal birefringence on ocular polarization," J. Opt. A: Pure Appl. Opt. **6**(3), S91–S99 (2004).
20. J. M. Bueno, "Measurement of parameters of polarization in the living human eye using imaging polarimetry," Vision Res. **40**(28), 3791–3799 (2000).
21. H. B. Klein Brink and G. J. Van Blokland, "Birefringence of the human foveal area assessed in vivo with Mueller-matrix ellipsometry," J. Opt. Soc. Am. A **5**(1), 49–57 (1988).
22. D. M. Maurice, "The structure and transparency of the cornea," J. Physiol. Paris **136**(2), 263–286 (1957).
23. A. Labbé, H. Liang, C. Martin, F. Brignole-Baudouin, J. M. Warnet, and C. Baudouin, "Comparative anatomy of laboratory animal corneas with a new-generation high-resolution in vivo confocal microscope," Curr. Eye Res. **31**(6), 501–509 (2006).
24. L. Kowalczuk, G. Latour, J. L. Bourges, M. Savoldelli, J. C. Jeanny, K. Plamann, M. C. Schanne-Klein, and F. Behar-Cohen, "Multimodal highlighting of structural abnormalities in diabetic rat and human corneas," Trans. Vis. Sci. Tech. **2**(2), 3 (2013).
25. D. Schulz, M. E. Iliev, B. E. Frueh, and D. Goldblum, "In vivo pachymetry in normal eyes of rats, mice and rabbits with the optical low coherence reflectometer," Vision Res. **43**(6), 723–728 (2003).
26. L. J. Bour and N. J. Lopes Cardozo, "On the birefringence of the living human eye," Vision Res. **21**(9), 1413–1421 (1981).
27. F. Beer, A. Wartak, R. Haindl, M. Gröschl, B. Baumann, M. Pircher, and C. K. Hitzenberger, "Conical scan pattern for enhanced visualization of the human cornea using polarization-sensitive OCT," Biomed. Opt. Express **8**(6), 2906–2923 (2017).
28. S. Bancelin, A. Nazac, B. H. Ibrahim, P. Dokladal, E. Decenciere, B. Teig, H. Haddad, H. Fernandez, M. C. Schanne-Klein, and A. De Martino, "Determination of collagen fiber orientation in histological slides using Mueller microscopy and validation by second harmonic generation imaging," Opt. Express **22**(19), 22561–22574 (2014).
29. K. M. Twietmeyer, R. A. Chipman, A. E. Elsner, Y. Zhao, and D. VanNasdale, "Mueller matrix retinal imager with optimized polarization conditions," Opt. Express **16**(26), 21339–21354 (2008).
30. J. F. De Boer, C. K. Hitzenberger, and Y. Yasuno, "Polarization sensitive optical coherence tomography–a review," Biomed. Opt. Express **8**(3), 1838–1873 (2017).
31. N. Lippok, M. Villiger, and B. E. Bouma, "Degree of polarization (uniformity) and depolarization index: unambiguous depolarization contrast for optical coherence tomography," Opt. Lett. **40**(17), 3954–3957 (2015).
32. G. J. van Blokland, "Ellipsometry of the human retina in vivo: preservation of polarization," J. Opt. Soc. Am. A **2**(1), 72–75 (1985).
33. J. M. Bueno and M. C. Campbell, "Polarization properties of the in vitro old human crystalline lens," Oph. Phys. Optics **23**(2), 109–118 (2003).

Biomedical Optics EXPRESS

34. M. C. Campbell, J. M. Bueno, C. J. Cookson, Q. Liang, M. L. Kisilak, and J. J. Hunter, "Enhanced confocal microscopy and ophthalmoscopy with polarization imaging," in *Photonic Applications in Biosensing and Imaging*, (International Society for Optics and Photonics, 2005), 59692H.
35. M. Bueno, J. J. Hunter, C. J. Cookson, M. L. Kisilak, and M. C. Campbell, "Improved scanning laser fundus imaging using polarimetry," J. Opt. Soc. Am. A **24**(5), 1337–1348 (2007).
36. J. M. Bueno and M. C. W. Campbell, "Confocal scanning laser ophthalmoscopy improvement by use of Mueller-matrix polarimetry," Opt. Lett. **27**(10), 830–832 (2008).
37. D. Lara and C. Dainty, "Double-pass axially resolved confocal Mueller matrix imaging polarimetry," Opt. Lett. **30**(21), 2879–2881 (2005).
38. D. Lara and C. Dainty, "Axially resolved complete Mueller matrix confocal microscopy," Appl. Opt. **45**(9), 1917–1930 (2006).
39. E. Compain, S. Poirier, and B. Drevillon, "General and self-consistent method for the calibration of polarization modulators, polarimeters, and mueller-matrix ellipsometers," Appl. Opt. **38**(16), 3490–3502 (1999).
40. I. Saytashev, S. Saha, J. Chue-Sang, P. Lopez, M. Laughrey, and J. C. Ramella-Roman, "Self validating Mueller matrix Micro–Mesoscope (SAMMM) for the characterization of biological media," Opt. Lett. **45**(8), 2168–2171 (2020).
41. P. J. Campagnola, A. C. Millard, M. Terasaki, P. E. Hoppe, C. J. Malone, and W. A. Mohler, "Three-dimensional high-resolution second-harmonic generation imaging of endogenous structural proteins in biological tissues," Biophys. J. **82**(1), 493–508 (2002).
42. J. Qi and D. S. Elson, "Mueller polarimetric imaging for surgical and diagnostic applications: a review," J. Biophotonics **10**(8), 950–982 (2017).
43. J. Trägårdh, G. Robb, R. Amor, W. B. Amos, J. Dempster, and G. McConnell, "Exploration of the two-photon excitation spectrum of fluorescent dyes at wavelengths below the range of the Ti: Sapphire laser," J. Microsc. **259**(3), 210–218 (2015).
44. J. R. Lakowicz, I. Gryczynski, H. Malak, M. Schrader, P. Engelhardt, H. Kano, and S. W. Hell, "Time-resolved fluorescence spectroscopy and imaging of DNA labeled with DAPI and Hoechst 33342 using three-photon excitation," Biophys. J. **72**(2), 567–578 (1997).
45. J. M. Dias and N. M. Ziebarth, "Anterior and posterior corneal stroma elasticity assessed using nanoindentation," Exp. Eye Res. **115**, 41–46 (2013).